Geochronology Discuss.,
https://doi.org/10.5194/gchron-2020-33-AC2, 2021

Interactive comment on "Uranium incorporation in fluorite and exploration of U-Pb dating" *by* Louise Lenoir et al.

Louise Lenoir et al.

louise.lenoir@universite-paris-saclay.fr

Received and published: 3 February 2021

We warmly thank Dr. Istvan Dunkl for his very constructive and detailed comments on our manuscript. The answer of authors (AA) is detailed after the reviewer's comment reminder (RC1) and can be found in PDF file.

RC1-"The fibrous texture is mentioned, but not documented. Add a microphotograph, with proper resolution, please." AA–> A new microphotograph has been added in Figure 3 of the preprint version (=Fig. 1 of reviewer's comment reply below). The fibrous texture is also visible in figure 4b (lower right), figure 6 (lower left), figure 11 (upper left), and figure A3.

RC1-"Line 63: In this sentence there is a paradox. You can argue that no other

geochronological method can be used in this paragenesis, thus the new results are unique and important. But you can not use it as a test site of the new method, when no other age control is available." AA–>This sentence has been modified as follows: "As in many other F-Ba deposits, the most commonly used geochronometers are lacking in Pierre-Perthuis making it an interesting target to gain knowledge on fluorite precipitation ages through fluorite U-Pb dating."

RC1-"You applied different laser beam diameters at the ablation analyses (40, 110, 135, 150, 155 μm are listed for different phases and different reference materials). This is a problematic point, as the fractionation, and its trend depend on the crater diameter and on the aspect ratio." AA–>Ablation parameters, including the laser beam diameter, indeed vary between reference materials and fluorite samples. We use NIST614 (pre-ablation: 135 μm, ablation: 110 μm) to correct all 207Pb/206Pb ratios. This correction is very small and does not depend much on the matrix and ablation diameter. 238U/206Pb ratios are corrected using WC-1. Ideally, a fluorite reference material should have been used. We have tested HK13 fluorite as a potential primary reference material. Unfortunately, these attempts to correct our 238U/206Pb ratios with HK13 fluorite were not conclusive, because (1) 238U/206Pb ratios vary within HK13 crystals, (2) The obtained isochron on HK13 is not satisfactory enough, and (3) the ablation crater aspect ratios vary between HK13 and Pierre-Perthuis fluorite samples, despite the fact that we used the same laser parameters (same ablation diameter, energy and repetition rate). Therefore, we used a non matrix-match primary reference material (RM) to correct all 238U/206Pb ratios. We used WC-1, a carbonate RM, but a zircon RM, such as 91500, could have been used as well (the problem would have been the same, i.e., no matrix-match primary RM to correct for 238U/206Pb). We have tested to ablate WC-1 with the same laser parameters used to ablate fluorite (pre-ablation: 110 μm, ablation: 85 μm, repetition rate: 8 Hz, fluence: 6.25 J.cm-2). Using these parameters, WC-1 ablation rate is variable, and as a result, the measured 238U/206Pb ratios are much more uncertain than usual. Moreover, the ablation crater aspect ratio was not comparable between WC-1 and fluorite, even though we used identical laser

parameters. Therefore, we used “standard” ablation parameters for WC-1 (pre- ablation: 155 μm, ablation: 150 μm, repetition rate: 8 Hz, fluence: 1 J.cm-2) to correct for 238U/206Pb. We do agree that applying this correction to our fluorite samples is problematic, because the crater aspect ratios differ between WC-1 and fluorite. Yet, this point is discussed in the text (section 5.2.2 “In situ LA-ICP-MS U-Pb dating”). The first sentence “In the absence of elemental fractionation correction against a fluorite RM, the age of the last generation of fluorite in Pierre-Perthuis ore (Flog2), 40.0 $\pm$ 1.7 Ma, may be over- or underestimated” in section 5.3 “U-Pb age significance”, also emphasizes the fact that our correction is uncertain. Using a laser beam diameter of 150 μm to ablate our fluorite samples was not an option, as the U-rich growth band is small (sometimes < 150 μm) and contain pyrite inclusions that must be avoided. In any cases, the problem would have remained the same: the aspect ratio is not comparable between WC-1 and fluorite, even when using the same ablation diameter.

RC1-"What was the use of the analysis of carbonate primary and secondary reference materials (WC-1, DBT and AUG-B6)? It is difficult to trace in the text that actually how was considered the observed matrix-controlled fractionation from the NIST glass isotope ratios and/or the deviation from the nominal ages. Why did you use at all carbonate?" AA–>NIST614 is used to correct 207Pb/206Pb ratios, the value being certified (0.8704, Jochum et Stoll, 2008). The 238U/206Pb value in NIST614 is not certified, and not used for correction. To properly correct all fluorite 238U/206Pb ratios, a fluorite RM showing comparable crater aspect ratios should have been used. Because such a fluorite RM is lacking, we used WC-1. Any other non matrix-match primary RM (e.g., Zircon 91500) could have been used instead of WC-1. Secondary calcite RM DBT and AUG-B6 are used to control the correction of 238U/206Pb ratios. Thanks to AUG-B6 and DBT, we show that the correction is valid for calcite. We fully agree that it does not mean that such a correction is valid for fluorite. Hence, correcting our fluorite 238U/206Pb ratios with a correction factor obtained from WC-1 calcite RM may introduce a bias (“In the absence of elemental fractionation correction against a fluorite RM, the age of the last generation of fluorite in Pierre-Perthuis ore (Flog2), 40.0 $\pm$ 1.7 Ma,

may be over- or underestimated” in section 5.3 “U-Pb age significance”). To evaluate the potential deviation from the nominal age, we used HK13 as a fluorite secondary RM. The correction factor for 238U/206Pb, based on WC-1, was applied to the measured HK13 238U/206Pb ratios, and an age of 285.9 $\pm$ 30.9 Ma is found. The idea was to introduce a second correction on all fluorite 238U/206Pb ratios, based on the deviation between our U-Pb age obtained on HK13, and the 290 $\pm$ 10 Ma (U–Th–Sm)/He age of Wolff et al. (2016). Unfortunately, the obtained U-Pb isochron on HK13 is not well defined, not allowing for a second correction of our fluorite 238U/206Pb ratios. To conclude, calcite RMs were used because of the lack of fluorite RM. We acknowledge that Figure A1 is confusing, mixing calcite and fluorite T-W diagrams. Therefore, we split this figure for clarity: in the article Figure A1 now shows T-W diagrams of calcite secondary RMs AUG-B6 and DBT, while Figure A2 shows the T-W diagram obtained on HK13 fluorite (see Fig.2 below).

RC1-" It is not clear, what is the penetration of the SR-XRF method. What volume supplies the chemical information, when the X-Y pixel size is 50 nm-1 μm, what is the Z dimension? Indicate it, please in the method section. E.g. in Figure 5 the Y pattern continues behind the pyrite inclusion, thus it seems that we got elementary signal from needle shaped volumes and not only from the surface. " AA–>The information depth of the XRF method is determined by the energy of measured characteristic X-ray line and composition of the absorbing matrix. The information depths of the most intense characteristic X-ray lines of the different elements have been calculated in CaF2 and are shown in the Fig. 3 below. We added in the main text this sentence: “Because we work on samples with a thickness of 100 to 300 microns, the low energy X-ray spectral line intensities will not be revealed from the whole sample thickness by SR-XRF. The depth of information for the elements included into the paper is documented in supplementary materials (see Table A2)” together with the new Table A2 (=Fig.3 in reviewer’s comment answer). Please notice that we have corrected Figure 8(=Fig.4 in reviewer’s comment answer), which did not contain the final intensity maps. The new modified Figure 8 includes the elemental intensity distributions with all the necessary

spectral corrections (spectral overlappings, escape and pile-ups). Finally, we add the spatial distribution of Fe in maps containing pyrite crystals. The different information depths of the different elements present in the pyrite can provide a rough estimation on the depth of the measured pyrite crystals, e.g. the XRF penetration depth of Fe in CaF2 is 18 μm. Hence, when Fe in pyrite is visible, the depth of the pyrite crystal included in fluorite is $\leq$ 18 μm. Since the XRF penetration depth of U is much higher (145 μm), a map such as the one illustrated in Figure 8 in the preprint version of the manuscript (=Fig. 4 below), showing Fe but no U in pyrite, reveal that no U was adsorbed onto the pyrite crystal surface. Moreover, all intensity maps were corrected for the intensity variation (< 10% peak-to-peak) of the exciting nano-beam during the experiment (e.g. Figure 11 in preprint version= Fig. 5 below).

RC1-"Figure 5: The Ca-plot needs some more explanation. It is not clear how linear is the colour scaling, and actually what is the meaning of the red-coloured horizontal patches at the top, only a few % Ca replacement or a non-Flt inclusion?" AA–>A monochromatic linear scale has been used to better illustrate the Ca repartition in this transect (Figure 5 in preprint version =Fig. 6 below). The original Ca map was indeed confusing, with horizontal Ca intensity zonation (with <10 % change of the Ca intensity) due to fluctuations in the I0 intensity of the focused X-ray beam. This ΔI0 intensity fluctuation is only visible in the maps of elements having relatively homogenous spatial distribution and high XRF intensity. Indeed, high (>10%) compositional inhomogeneity provides a proportionally stronger than 10% intensity variation in the elemental distribution maps hiding the effect of ΔI0. On the other hand, for low (<100 counts) XRF signals, the statistical fluctuation of the signal is higher than 10%. Regarding the horizontal patch at the top of the Ca map, it could either correspond to an empty tiny fracture or to a fracture filled with barite (not verified). Fig. 7 is a photograph (to the left) and a SEM image (to the right) illustrating this late barite stage, growing on top of fluorite and in microfractures.

RC1-"The globular shape of the tiny pyrite crystals is not convincing. The zonation

of the pyrite in Figure 9 can also be interpreted as cube + a small octahedron at the corners." AA–>We agree that some crystallographic structures are visible in Figure 9 of the preprint version, revealed by elemental zonation. However, we propose to keep the term “globular”, referring to the morphology of the crystals when observed under the optical microscope. Fig. 8 is a compilation of microphotographs: although we can sometimes see sharp angles evocating cubes and octahedrons, most crystals do not exhibit clear structures.

RC1-"I would suggest to replace in many sentences "metal" by "element". Please scan through the text." AA–>We agree and modify the text accordingly.

RC1-"Figure 10. should be re-designed; e.g. explain better on the figure the "redox front". " AA–>A new version is proposed in the reviewed manuscript (see Fig. 9).

RC1-"What can be the source of the F? Do you assume an external, F rich brine, or it can be related to the breakdown of biotite locally, in the granitoid basement? " AA– >Although a contribution of F-rich sedimentary brines cannot be excluded, we think that biotite dissolution and recrystallization into chlorite is the main source of F. REE distribution in fluorite (unpublished data from the PhD dissertation of Gigoux, 2015, university Paris-Sud) show that mineralizing fluids interacted with the granite basement. Fig.10 is a microphotograph of a chloritized biotite in granite fragments closely associated to geodic fluorite (width ca. 1mm).

RC1-"Line 391: "As the thickness of these bands is sometimes less than 10 μm, we suggest that the coloration was acquired through gamma irradiation, instead of α-irradiation, which would have caused larger bands" It is a very wild statement, as the penetration of gamma ray is much longer than the alpha particles. Without any detailed explanation and citations this assumption is not tenable." AA–>We agree and would like to clarify this point. We initially suspected that purple coloration was acquired through internal α-irradiation. Even though U and Th have been sometimes detected in these purple layers (Figure 11 in preprint version), this is not systematic (Figures 5 and

8 of the preprint version). Moreover, some purple layers are less than 10 μm, which seems too small if explained by internal α-irradiation. Finally, the most external growth band, in which U and Th are present, is translucent. We have therefore excluded the hypothesis of internal α-irradiation, and we propose instead a coloration acquired by external γ-irradiation. This sentence is now reformulated in the revised version of the manuscript: “Because the width of such bands is sometimes less than 10 μm, we have discarded the hypothesis of a coloration acquired through internal alpha irradiation (Dill and Weber, 2010; Pi et al., 2007; Vochten et al., 1977). Moreover, it must be noted that such coloration is not developed in the U-bearing Flog2 layer (Figures 6 and 8 of the preprint version). We rather suggest that coloration was acquired through external gamma irradiation.”

RC1-"Figure 11: The incorporation of Zr in the fluorite lattice is highly interesting and in the first glance rather difficult to explain. Add maybe some sentences about it." AA–>The Zr SR-XRF maps show the Zr intensity above the detection limit of 99% confidence level (3σ of the background below the Zr peak). We do agree that Zr incorporation should be discussed in the studied fluorite overgrowth as illustrated in Figures 8 and 11 in the preprint version. We do not have information regarding the physical-chemical properties of the fluid in which Zr (and U) was dissolved and transported. We also do not have information regarding how Zr is incorporated in the fluorite lattice. However, we take this opportunity to discuss the potential origin of Zr. The fluid temperature is not known (no fluid inclusions, as illustrated in Figure A2), but was likely < 100 âŮęC as discussed in the manuscript. At such low temperatures, zircon dissolution can be ruled out. A possible source of Zr (and U?) is the leaching of volcanic glasses. Late Variscan ignimbrites are cropping out ca. 35 km south of Pierre-Perthuis (Carpena et al., 1984). Partial dissolution of volcanic glass was identified as a source of Zr-U miner- alization in the Akouta Uranium deposit in Niger (Forbes et al., 1984), in the Kurupung batholith in Guyana (Cinelu and Cuney, 2006), and in the Tim MersoìĹ Basin in the Ebba deposit in Niger at temperatures below 200 âŮęC (Pons, 2015). This discussion is added in the revised version of the manuscript, in section 5.1 “Uranium

and lead incorporation in fluorite”: “...On a smaller scale, SR-XRF reveals micrometer-scale fluctuations in uranium concentrations along the growth directions, correlated with the incorporation of other substituted elements such as Sr and Zr (Figure 8). The incorporation of Zr in the fluorite lattice, together with U, may reflect a contribution from the leaching of volcanic glasses. Indeed, correlations between uranium and zirconium concentrations have been documented in various U deposits spatially associated to volcanic rocks or volcanic fragments reworked in sandstones and conglomerates (Forbes et al., 1984; Cinelu and Cuney, 2006; Pons, 2015). Late Variscan ignimbrites are cropping out ca. 35 km south of Pierre-Perthuis (Carpena et al., 1984).”

RC1-"Line 400: Lead "seems to be correlated with Th". Just by visual observation it is difficult to evaluate, e.g. the U & Pb seems to be also correlated. Supposedly the SF-XRF data are not quantitative, but I guess that from the pixel intensities it would be possible to generate X-Y plots (having arbitrary, but linear scales) that may show correlations and trends between elements. Then the word "correlation" can be used at a higher significance." AA–>We thank Istvan Dunkl for this suggestion. We add in supplementary materials (Figure A5, reproduced below) a cross-plot illustrating (in pixel intensity) lead as function of thorium (blue) and uranium (red). This sentence is now reformulated in the revised version of the manuscript: “Lead was detected by SR-XRF mapping, and its distribution in Flog2 is correlated with Th (Figures 6 and 11) but not with uranium (Figure A5). During the co-precipitation of pyrite and Flog2, lead was preferentially incorporated into pyrite crystals (Figure 8).” See X-Y plots in Fig. 11.

RC1-"Line 406: "To test the reliability of U-Pb dating in the fluorite rims of Pierre-Perthuis, we further discuss potential alterations by (1) the development of fractures and cleavages;" But in line 412: "these fractures only generated local alterations and were consequently avoided in LA-ICP-MS analyses". It means that the reliability was actually not tested, just the most intact volumes were considered for analyses. I recommend the rejection from the text the goal formulated in Line 406 as it was not fulfilled. Similarly, from Line 413, it is not the test of reliability." AA–>This sentence has been

reformulated in the revised version of manuscript: "We further discuss potential alterations of the U-Pb geochronometer by (1) the development of fractures and cleavages; (2) dissolution and re-crystallization; (3) solid-state diffusion."

RC1-"Line 484: It is difficult to accept your view to consider two dates (ca. 130 and ca. 40 Ma) as the "lifetime" of the deposit was 90 Ma (better Myr) long. They can also be interpreted as two independent fluid circulation+mineralization events." AA–>Two sentences were modified in section “5.3.2 Wider considerations regarding radiometric dating of ore deposits”: - “Hence, successive mineralizing fluids occur during a time period of ca. 90 Ma.” “Hence, at least two mineralizing events occur during a time period of ca. 90 Ma.” - “A late Eocene age estimate for the last fluorite-mineralizing event reveals that the “lifetime” of the deposit was much longer than previously thought.” “A late Eocene age estimate for the last fluorite-mineralizing event reveals that the ore formation is polygenic.”

RC1-"I am just speculating, what is actually the speciality of this deposit having two phases of fluorite crystallisation. If we think about the regional events, the ca. 130 Ma would fit perfectly to the maximum burial and thermal climax of the basin and the Eocene age would fit well to the impact of the descendent meteoric, oxidative fluids. The former was reductive, thus no U mobilization had happened, while the second regime contributed to the further breakdown of biotites by oxidation and could carry U. It is only a guess." AA–>The revised version of our conceptual model (Fig. 9) now illustrates the lithostratigraphic columns of the Pierre-Perthuis area at 130 Ma and 40 Ma.

RC1-"The suggested biogenic process-triggered change in eH is a plausible explanation, although not fully proven. Add, please in the text the calculated/measured basin-bottom burial temperature in Eocene time. It can be used as argument that the paleo-temperature did not exclude the bacterial activity." AA–>Barbarand et al., 2013, used apatite fission track thermochronology to show that the basement of the southeastern Paris Basin was subjected to temperatures less than 60 âŮęC during Eocene. This is

correlated with the paleodepth estimation of the Jurassic cover in the east of the Paris basin (400 to 500 meters) during the Eocene by calcite twinning and faulting by Rocher et al., 2004. Taking into account the present-day thermal gradient (ca. 30 âŮęC per km), this indicates a range of temperature compatible with the viability of bacteria. A lithostratigraphic column of the Pierre-Perthuis area during the Eocene period is now included in new Figure 10 of the article (=Fig. 9 in reviewer’s comment answer).

RC1- "the density contrast between the glass and the fluorite should be considered, as the ranges of fission particles are different" AA–>We have taken this comment into consideration to correct uranium concentrations in our fluorite samples. This correction is added in the revised version of the manuscript, in section 3.3 “Uranium distribution mapping”: "Enkelmann et al, 2005 have documented that the correction factor for uranium concentration between a standard and any unknown geological material depends on the range of latent track lengths and the density of materials. The latent track lengths of fission particles (2R) have been simulated using SRIM® software (Ziegler et al., 2010). Numerical data employed and results of these simulations are summarized in Table A1 (see supplementary materials). The calculated correction factor (Fcorr) for uranium concentration in fluorite is 0.866." We also detailed our method in the supplementary materials and added this discussion: "The range of latent track lengths of fission particles (2R) depends on the density of materials (Enkelmann et al., 2005). The latent fission-track lengths correspond to the combined ranges of the light and heavy nuclides ejected in opposite directions from the fission of 235U after capture of a thermal neutron (Joncheere, 2003). 2R in fluorite has been simulated using SRIM® software (Ziegler et al., 2010). Mass and energy values of fission products are taken from Kahn et Forgue (1967) and glass standard reference CN5 density from DeCorte et al., 1998. All data and simulations results are summarized in Table A1." Table A1 in revised version of the manuscript=Fig.12 in reviewer’s comment answer

RC1-"Figure A3: This SEM images unfortunately are not informative and not proper. Replace them by other SEM images that show the craters in an oblique view without

any overlay (please no blue staining and circles). It would be crucial to document that using the applied ablation settings the craters have been developed by a continuous ablation and they have regular U-profile or the formation mechanism was a sequence of explosions and the bottom has irregular, fractured, zig-zag shape. AA–>We replaced the SEM images by new images acquired using optical profilometry, to correctly estimate the ablated volume and crater aspect ratio. " We added the following sentence in the text: “We document four examples of LA-ICP-MS intensity signals during fluorite ablation together with the corresponding 3D surface images of laser craters acquired by optical profilometry (see Figure A4 and detailed methodology in supplementary materials).” Figure A3 in preprint version of the manuscript=Fig.13 in reviewer’s comment answer The following section is added in supplementary materials: “3D images of laser craters in fluorite have been acquired using an optical profilometer 3D Contour GT-X (Bruker Corp., Billerica, MA, USA) in VSI (Vertical Shift Interference) mode at GeePs laboratory, University Paris-Saclay. This instrument produces 3D images of a surface and also depth profiles on chosen axes thanks to Vision® analysis software (VISIONx Inc., Pointe Claire, Quebec, Canada). The VSI mode is based on white light vertical scanning interferometry, with measurable topography up to 1 mm and a vertical resolution of 3 nm. Lateral resolution measurements are a function of the objective magnification (a $\times$50 magnification was used for this study) giving a lateral resolution of 0.2μm.”

RC1-"Table A3: Two columns can be deleted (surface of the sample & bottom of the crater), as these are unimportant raw data. The craters are very deep, and their aspect ratio seems to be not usual at LA geochronology. In case of such deep craters the down-hole fractionation can be extremely high." AA–>This Table A3 has been replaced by optical profilometer measurements of crater depth and calculated ablated volume (see answer to previous remark for details) =Fig. 14

RC1-"Review_Fig. 1; Left panel: WC1-20191219 sample as it is presented in the supplementary Excel file, Right panel: all data plotted by IsoplotR. Could you please

explain the selection criteria applied at the reduction from the total 45 data to 23 that were used. " AA–>During this sequence, we have tested different ablation parameters on WC-1, so as to use identical beam diameter, energy and repetition between WC-1 and fluorite samples (85 μm, 6.25 J.cm-2, 8 Hz). As discussed above, uncertainties measured on WC-1 238U/206Pb and 207Pb/206Pb ratios were much higher than those obtained using lower energy and larger beam diameter (150 μm, 1 J.cm-2, 8 Hz) and we have decided to discard all 19 WC-1 analysis at 85 μm, 6.25 J.cm-2, 8 Hz and keep the analysis at 150 μm, 1 J.cm-2, 8 Hz. These 19 discarded analyses were included by mistake in the spreadsheet and are now removed from the revised version. In addition, 3 analyses (out of 26) performed at 150 μm, 1 J.cm-2, 8 Hz were discarded because of very unusually high lead signal intensity indicating contamination. During this sequence, average 206Pb intensity for these 3 discarded analyses is 61000 cps/s while the average of the 23 other analyses is 4400 cps/s. Similarly, the average signal in 207Pb for the 3 excluded analyses is 30 times higher than the average of the 23 other analysis. The consequence is abnormally high 207Pb/206Pb ratios.

RC1-"Review_Fig. 2; Left panel: AUG-B6-20191219 sample as it is presented in the supplementary Excel file, Right panel: data plotted by Isoplot R considering at the input 2 se for the uncertainties. The error ellipses are different (see just above the number "50"). Control, please, this deviation; at the input the uncertainty should be set according to the data table." AA–>The 21st spot on B6 of sequence 2019.12.20 has been deleted by error. The corrected T-W diagram, including spot #21, and the corrected age and associated uncertainty, is now included in the figure and text. The corrected figure is reproduced in Fig.2.

Bibliography Carpéna, J., Doubinger, J., Guérin, R., Juteau, J. and Monnier, M.: Le volcanisme acide de l’ouest-morvan dans son cadre géologiqueâĂŕ: caractéristique géochimique, structurale et chronologique de mise en place, Bulletin de la Société Géologique de France, (5), 839–859, 1984. Cinelu, S. and Cuney, M.: Sodic metasomatism and U–Zr mineralization: A model based on the Ku-

rupung batholith (Guyana), Goldschmidt conference, 1, 2006. De Corte, F., Simonits, A., De Wispelaere, A. and Hoste, J.: Accuracy and applicability of the k0-standardization method, Journal of Radioanalytical and Nuclear Chemistry, Articles, 113(1), 145–161, https://doi.org/10.1007/BF02036056, 1987. Dill, H. G. and Weber, B.: Accessory minerals of fluorite and their implication regarding the environment of formation (Nabburg–Wölsendorf fluorite district, SE Germany), with special reference to fetid fluorite ("Stinkspat"), Ore Geology Reviews, 37(2), 65–86, https://doi.org/10.1016/j.oregeorev.2010.01.004, 2010. Enkelmann, E., Jonckheere, R. and Ratschbacher, L.: Absolute measurements of the uranium concentration in thick samples using fission-track detectors, Nuclear Instruments and Methods in Physics Research Section B: Beam Interactions with Materials and Atoms, 229(3–4), 489–498, https://doi.org/10.1016/j.nimb.2005.01.003, 2005. Forbes, P., Pacquet, A., Chantret, F., Oumarou, J. and Pagel, M.: Marqueurs du volcanisme dans le gisement d'uranium d'Akouta (République du Niger), Comptes Rendus de l'Académie des Sciences - Series II - Earth and Planetary Science, 647–650, 1984. Gigoux, M.: Origine des minéralisations stratiformes de fluorine de la bordure sud-est du bassin de Paris, , 307, n.d. Gigoux, M., Delpech, G., Guerrot, C., Pagel, M., Augé, T., Négrel, P. and Brigaud, B.: Evidence for an Early Cretaceous mineralizing event above the basement/sediment unconformity in the intracratonic Paris Basin: paragenetic sequence and Sm-Nd dating of the world-class Pierre-Perthuis stratabound fluorite deposit, Mineralium Deposita, 50(4), 455–463, https://doi.org/10.1007/s00126-015-0592-1, 2015. Jochum, K. P. and Stoll, B.: Chapter 10: Reference materials for elemental and isotopic analyses by LA-(MC)-ICP-MS: success and outstanding needs, , 22, n.d. Jonckheere, R.: On the densities of etchable fission tracks in a mineral and co-irradiated external detector with reference to fission-track dating of minerals, Chemical Geology, 200(1–2), 41–58, https://doi.org/10.1016/S0009-2541(03)00116-5, 2003. Kahn, S. and Forgue, V.: Range-Energy Relation and Energy Loss of Fission Fragments in Solids, Phys. Rev., 163(2), 290–296, https://doi.org/10.1103/PhysRev.163.290, 1967. Pi, T., Solé, J., Golzarri, J., Rickards, J. and Espinosa, G.: Autoradiography of geological fluorite

samples for determination of uranium and thorium distribution using nuclear track methodology, Revista mexicana de física, 53, 57–60, 2007. Pons, T.: Caractérisation des oxy-hydroxydes de fer et des éléments associés (S, Se, As, Mo, V, Zr) dans les environnements redox favorables aux gisements d'uranium, , 280, n.d. Roberts, N. M. W., Rasbury, E. T., Parrish, R. R., Smith, C. J., Horstwood, M. S. A. and Condon, D. J.: A calcite reference material for LA-ICP-MS U-Pb geochronology, Geochemistry, Geophysics, Geosystems, 18(7), 2807–2814, https://doi.org/10.1002/2016GC006784, 2017. Rocher, M., Cushing, M., Lemeille, F., Lozac'h, Y. and Angelier, J.: Intraplate paleostresses reconstructed with calcite twinning and faulting: improved method and application to the eastern Paris Basin (Lorraine, France), , 21, 2004. Vochten, R., Esmans, E. and Vermeirsch, W.: Study of the solid and gaseous inclusions in the fluorites from Wölsendorf (Bavaria, F.R. of Germany) and Margnac (Haute Vienne, France) by microprobe and mass spectrometry, Chemical Geology, 20, 253–263, 1977. Wolff, R.: Fluorite (U-Th-Sm)/He thermochronology, , 103, 2015. Ziegler, J. F., Ziegler, M. D. and Biersack, J. P.: SRIM – The stopping and range of ions in matter (2010), Nuclear Instruments and Methods in Physics Research Section B: Beam Interactions with Materials and Atoms, 268(11–12), 1818–1823, https://doi.org/10.1016/j.nimb.2010.02.091, 2010.

Please also note the supplement to this comment:
https://gchron.copernicus.org/preprints/gchron-2020-33/gchron-2020-33-AC2-supplement.pdf

---

Interactive comment on Geochronology Discuss., https://doi.org/10.5194/gchron-2020-33, 2020.

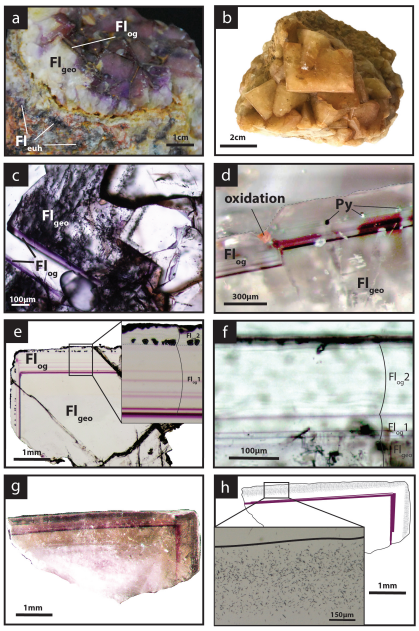

Fig.1 : Photographs of the fluorite stages from the Pierre-Perthuis ore. (a) Geode in the altered granite with milky white cubic crystals (Flgeo) and the translucent fluorite overgrowth (Flog) delimited by a thin purple band. The euhedral fluorite (Fleuh) forms patches in the Avallon granite, from Gigoux et al., 2015 , (b) Centimetric cubes of Flgeo, (c) Transmitted light microscopy photography of Flgeo and the overgrowth corresponding to Flog, (d) Photography of the limit between Flgeo and Flog with a pyrite crystal affected by a fracture and oxidized, (e) Transmitted light microphotograph of a geodic fluorite crystal with the two stages constituting Flog (1) a translucent fluorite initiated by one or several purple rims: Flog1; (2) a final growth stage of laminar fibrous fluorite with pyrite inclusions: Flog2, (f) Microphotograph in transmitted light showing the fibrous texture of Flog2 (g) Photography in transmitted light of an irradiated crystal of Flgeo + Flog, (h) Corresponding interpreted map of the induced fission tracks distribution in a crystal illustrated in (g) with a zooming on the muscovite detector.

Fig. 1.

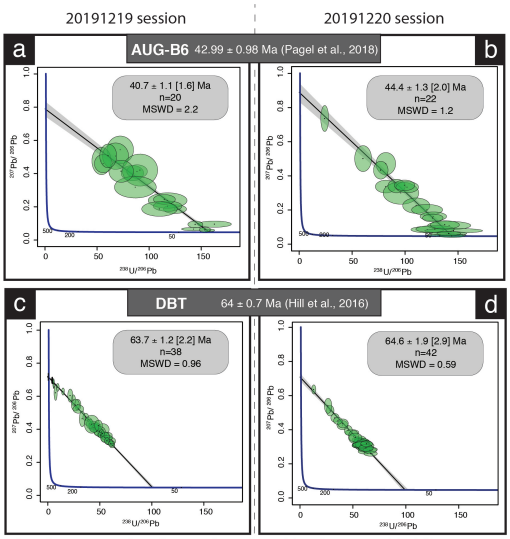

Figure A1: Tera-Wasserburg diagrams of secondary calcite reference materials. (a,b) Tera-Wasserburg diagrams displaying corrected ages for the calcite of the Gondrecourt graben AUG-B6 measured during the two analytical sessions, (c,d) Tera-Wasserburg diagram displaying the Duff Brown Tank corrected ages measured during the two analytical sessions.

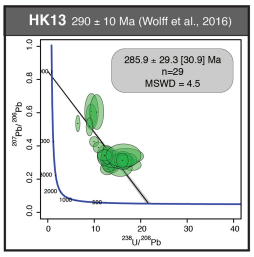

Figure A2: Tera-Wasserburg diagrams of secondary fluorite reference materials, "HK13" dated at 290 ± 10 Ma by Wolff et al., 2016.

Fig. 2.

Element	X-ray line, (in keV)	CaF_2, information depth, (in μm)
S	2,3	5,5
Ca	3,691	20
Fe	6,403	18
Y	14,957	189
Sr	14,164	162
Zr	15,774	220
U	13,613	145
Pb	10,549	70
Th	12,966	126

Fig. 3: Information depth estimation (in µm) and measured X-ray line (in keV) of the SR-XRF method in fluorite for each element included into the paper.

Fig. 3.

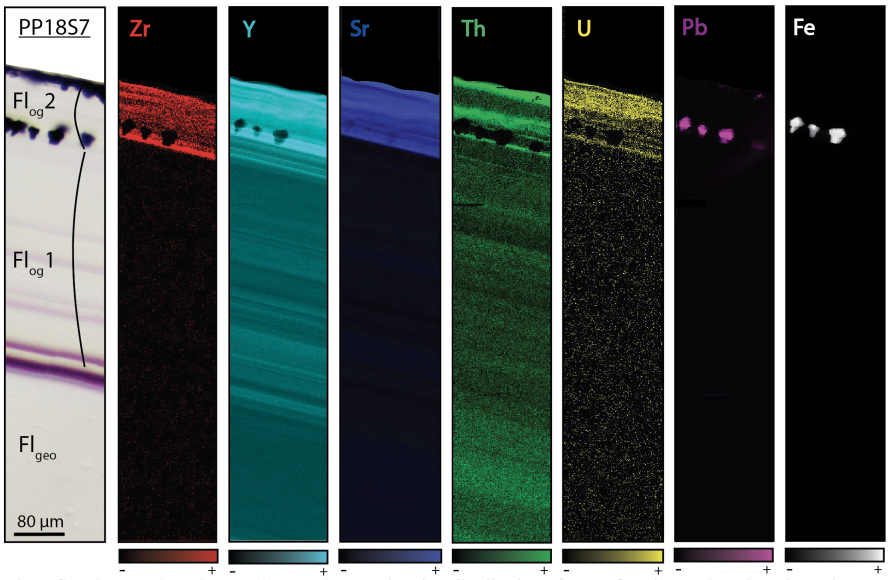

Fig.4: Synchrotron-based XRF elemental maps showing distribution of Zr, Y, Sr, Th, U, Pb and Fe through a transect from the core crystal Flgeo to the Flog rim of PP18S7. Color bars indicate intensity scale (black indicates concentrations below the detection limit). Higher intensities correspond to higher element contents. Map dimensions are 179µm x 1mm.

Fig. 4.

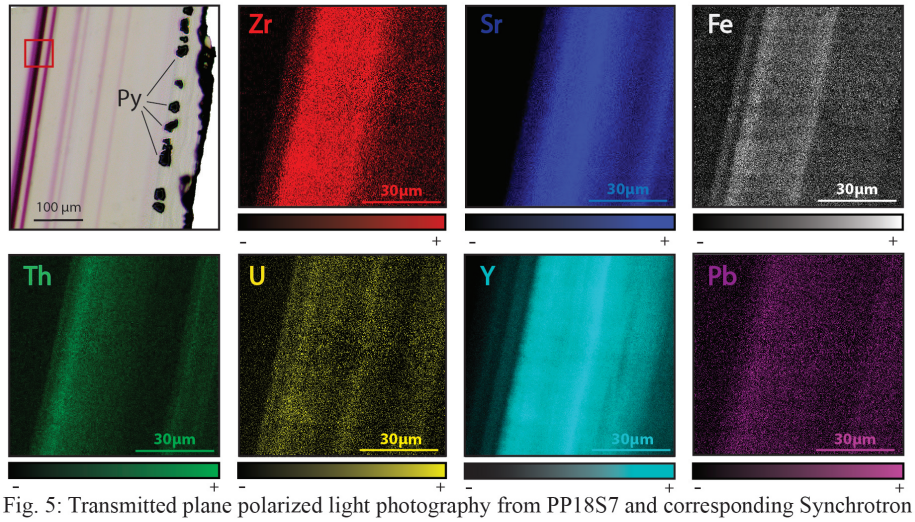

Fig. 5: Transmitted plane polarized light photography from PP18S7 and corresponding Synchrotron X-ray fluorescence elemental maps. Area of XRF scan is outlined by a red box on the photography. Map dimensions are 80 x 80 µm.

Fig. 5.

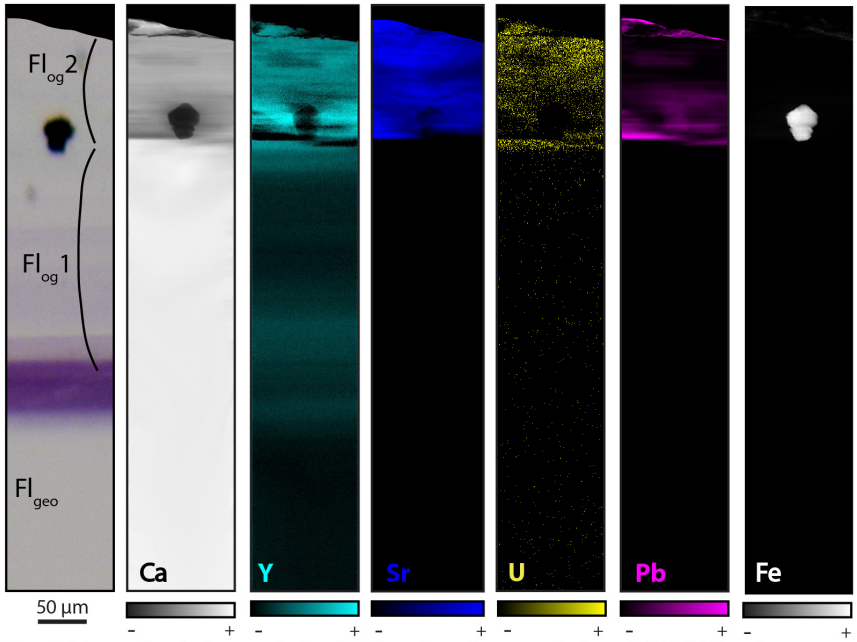

Fig. 6: Transmitted plane polarized light microphotograph from PP18S15 and corresponding synchrotron radiation X-ray fluorescence elemental maps. Black areas indicate concentration below the limit of detection of the element. A globular pyrite crystal is included in Flog2.

Fig. 6.

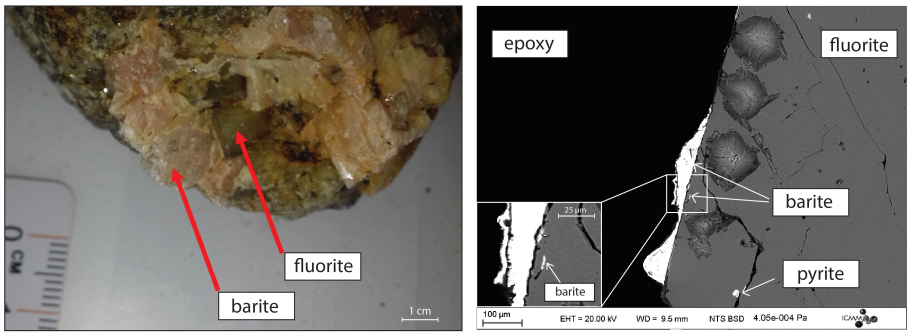
fluorite
barite
1 cm
epoxy
fluorite
barite
pyrite
barite
25 µm
100 µm
EHT = 20.00 kV
WD = 9.5 mm
NTS BSD
4.05e-004 Pa

Fig. 7.

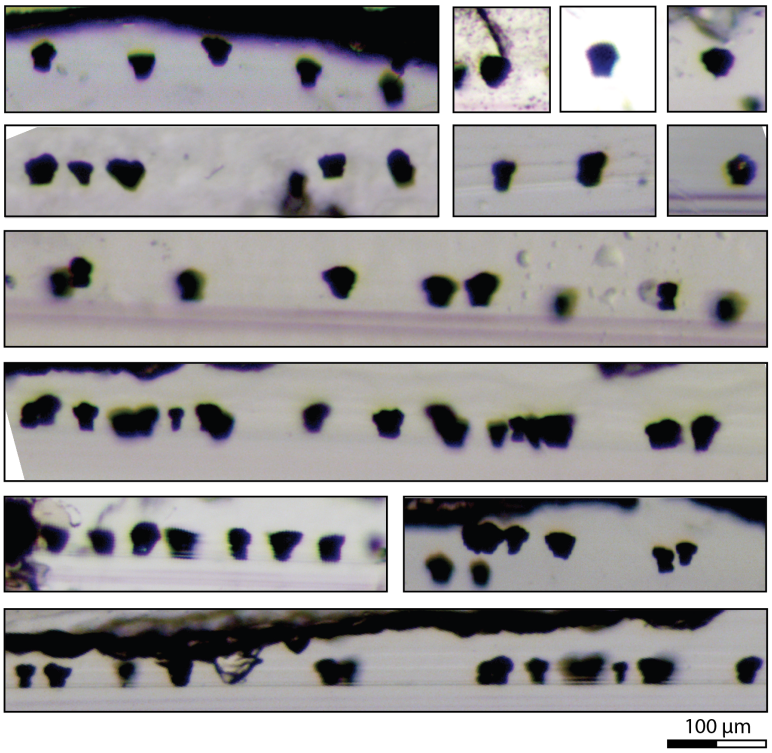
100 µm

Fig. 8.

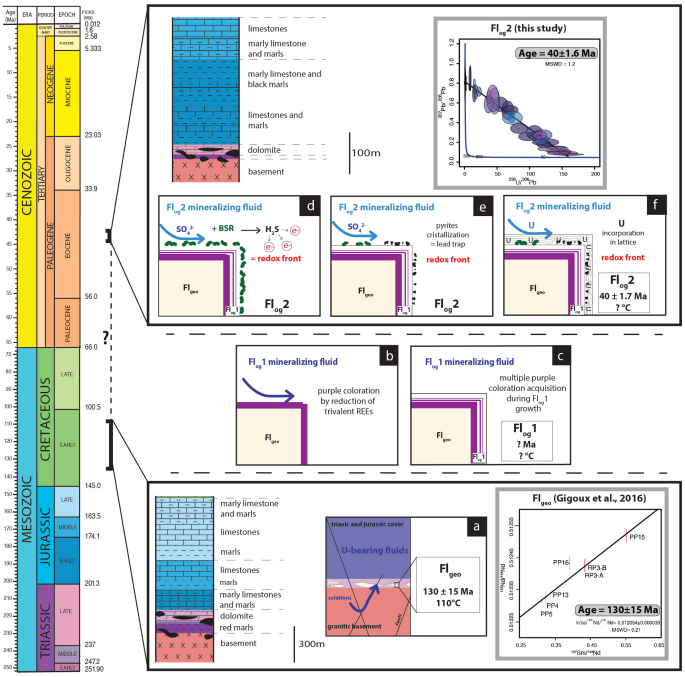

Fig. 9: Conceptual model of uranium incorporation in the fluorite lattice. a) Uranium is leached by F-rich solutions flowing through the granitic basement and reaching Flgeo in the basement/cover interface, b) formation of purple layers on the fluorite surface by F-bearing fluids, c) crystallization of Flog1, d) a local redox front is generated by BSR, e) sulfur species react with iron oxyhydroxides or dissolved Fe to form pyrite, f) uranium is incorporated in Flog2.

Fig. 9.

Fig.10: Microphotograph of a chloritized biotite in granite fragments closely associated to geodic fluorite (width ca. 1mm)

Fig. 10.

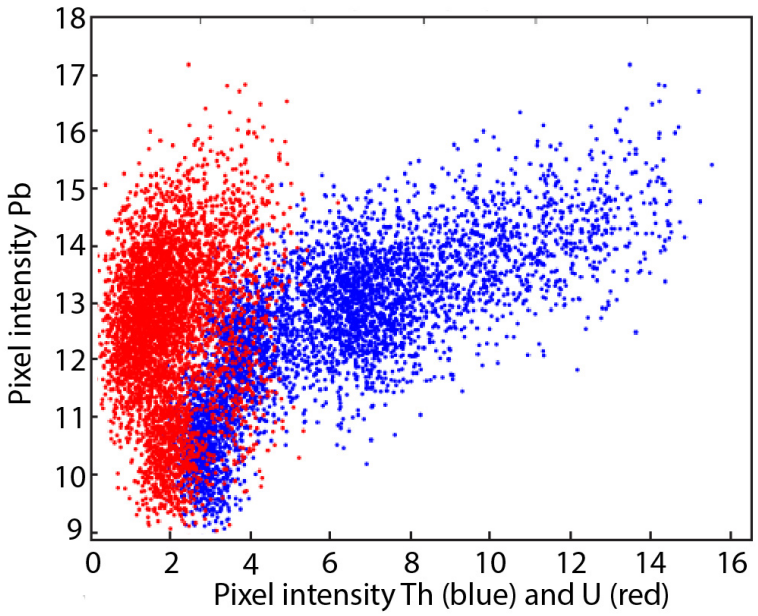

Fig. 11: Scatter plot of lead as function of thorium (blue) and uranium (red) in pixel intensities.

Fig. 11.

(a) Projectiles	**Z**	**M_A (amu)**	**E_0 (MeV)**
Hv (Xe)	54	138.1	69.6
Lt (Sr)	38	95.34	100.1
(b) Matrices	**Formula**	**d (g.cm3)**	
Glass CN5	SiO_2	2.45	
Fluorite	CaF_2	3.18	
(c) Simulations	**Range Hv (μm)**	**Range Lt (μm)**	**[2R]**
Glass CN5	10.5	14.7	25.2
Fluorite	9.5	12.9	22.4
(d) Correction factor	**$d_{Glass\ CN5}/d_{Fluorite}$**	**$[2R]_{Glass\ CN5}/[2R]_{Fluorite}$**	**F_{corr}**
Glass CN5/Fluorite	0.770	1.125	0.866

Fig. 12: Data used to calculate the correction factor for uranium concentration in fluorite using induced fission track mapping in SRIM® software. a) mass (MA) and energy (E0) of heavy (Hv) and light (Lt) nuclides produced by the fission of 235U, b) Formula and density (d) of the two simulated materials, c) Latent track lengths (2R) obtained by adding both nuclides simulated range lengths, (d) uranium concentration correction factor (Fcorr) calculated for fluorite with glass standard material (Enkelmann et al., 2005).

Fig. 12.

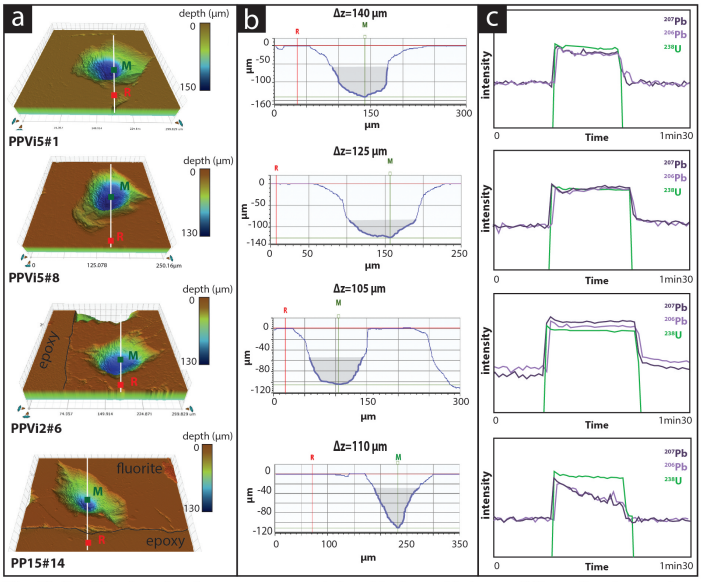

Fig. 13: Qualification of various crater aspects induced by laser ablation on different fluorite sample a) 3D surface images of craters reconstructed by optical profilometer, b) corresponding 2D axial section with the measurement of crater depth thanks to two markers: R (the average value of the topography near to the crater) and M (the deepest point in the crater) expressed as Δz in µm. In grey is illustrated the volume below a diameter of 85µm, corresponding to the acquired ablation sequence, while the upper crater volume corresponds to fragments ejected and material ablated during the pre-ablation sequence, c) corresponding LA-ICP-MS signal intensity of 238U, 206Pb and 207Pb during the acquisition sequence. Analyses PPVi5#8, PPVi5#1 and PPVi2#6 were included in the Tera-Wasserburg diagrams, while PP15#14 is an example of analysis discarded due to variable 238U/206Pb.

Fig. 13.

Sample	Total depth, including pre-ablation (μm)	Total volume, including pre-ablation (μm^3)
PPVi2_#13	130	574842
PPVi2_#19	116	675090
PPVi2_#24	145	818605
PPVi2_#25	105	626830
average	124	673842
PPVi5_#1	140	875287
PPVi5_#2	140	912850
PPVi5_#3	120	834602
PPVi5_#8	125	757431
average	131	845043
PP1802_#6	103	524342
PP1802_#9	110	507250
PP1802_#11	122	549564
PP1802_#12	132	621271
average	117	550607
PP15_#3	105	249329
PP15_#9	110	329296
PP15_#14	110	360308
PP15_#15	130	451288
average	114	347555
HK13#1#5	210	N.D.

Fig. 14: Statistical analysis of crater depths induced by laser ablation for U-Pb dating by optical profilometer. The total crater depths and volumes include the 7s pre-ablation.

Fig. 14.